JGR Earth Surface

RESEARCH ARTICLE
10.1029/2021JF006281

Key Points:

- To understand the structure beneath the land surface, we constructed a three-dimensional P-wave velocity model of a shale watershed
- The spatially varying depth of mobile soil and the onset of dissolution of chlorite were mapped based on Vp of 600 and 2,700 m/s
- The subsurface structure represents the long-term integrated effect of water-induced weathering responding to both climate and topography

Supporting Information:

Supporting Information may be found in the online version of this article.

Correspondence to:

W. Wang,
wangxiawei0619@gmail.com

Citation:

Wang, W., Nyblade, A., Mount, G., Moon, S., Chen, P., Accardo, N., et al. (2021). 3D seismic anatomy of a watershed reveals climate-topography coupling that drives water flowpaths and bedrock weathering. *Journal of Geophysical Research: Earth Surface*, *126*, e2021JF006281. https://doi.org/10.1029/2021JF006281

Received 26 MAY 2021
Accepted 30 NOV 2021

Author Contributions:

Conceptualization: Wei Wang, Andrew Nyblade, Xin Gu, Susan L. Brantley
Data curation: Wei Wang, Greg Mount, Natalie Accardo, Brandon Forsythe
Funding acquisition: Susan L. Brantley
Methodology: Wei Wang, Seulgi Moon, Po Chen
Supervision: Andrew Nyblade, Susan L. Brantley
Visualization: Wei Wang
Writing – original draft: Wei Wang
Writing – review & editing: Wei Wang, Andrew Nyblade, Seulgi Moon, Xin Gu, Susan L. Brantley

3D Seismic Anatomy of a Watershed Reveals Climate-Topography Coupling That Drives Water Flowpaths and Bedrock Weathering

Wei Wang[1], Andrew Nyblade[1], Greg Mount[2], Seulgi Moon[3], Po Chen[4], Natalie Accardo[1], Xin Gu[1], Brandon Forsythe[1], and Susan L. Brantley[1,5]

[1]Department of Geosciences, Penn State University, University Park, PA, USA, [2]Department of Geoscience, Indiana University of Pennsylvania, Indiana, PA, USA, [3]Department of Earth, Planetary and Space Sciences, University of California, Los Angeles, Los Angeles, CA, USA, [4]Department of Geology and Geophysics, University of Wyoming, Laramie, WY, USA, [5]Earth and Environmental Systems Institute, University Park, PA, USA

Abstract To investigate how bedrock transforms to soil, we mapped the topography of the interface demarcating onset of weathering under an east-west trending shale watershed in the Valley and Ridge province in the USA Using wave equation travel-time tomography from a seismic array of >4,000 geophones, we obtained a 3D P-wave velocity (Vp) model that resolves structures ~20 m below land surface (mbls). The depth of mobile soil and the onset of dissolution of chlorite roughly match Vp = 600 m/s and Vp = 2,700 m/s, respectively. Chlorite dissolution initiates porosity growth in the shale matrix. Depth to the 2,700 m/s contour is greater under the N- as compared to S-facing hillslopes and under sub-planar as compared to concave-up land surfaces. Broadly, the geometries of the 'soil' and 'chlorite' Vp contours are consistent with the calculated potential for shear fracture opening under weak regional compression. However, this calculated fracture potential does not consistently explain observations related to N- versus S-facing aspect nor fracture density observed by borehole televiewer. Apparently, regional compression is only a secondary influence on Vp: the primary driver of P-wave slowing in the upper layers of this catchment is topographic control of reactive water flowpaths and their integrated effects on weathering. The Vp result is best explained as the long-term integrated effect of groundwater flow-induced geochemical weathering of shale in response to climate-driven patterns of micro- and macro-topography.

Plain Language Summary Our capacity to understand the subsurface structure that controls storage and flow of groundwater relies largely on point measurements at boreholes and outcrops. In this study, we developed understanding of the subsurface structure beneath a shale watershed in three-dimensions (3D) by using a dense seismic array of >4,000 geophones. We obtained a 3D P-wave velocity model with resolution to image ~20 m below the land surface. By correlating our velocity structures to borehole logs and geochemical measurements at the same site, we were able to explore the "landscape" defined by the bottom of the mobile soil and the onset of porosity growth by clay weathering. This 3D image shows how the depth of soil and onset of dissolution varies with orientation with respect to the sun (aspect) and as a function of planar versus concave-up land surfaces (curvature). Some of the subsurface structure can be explained by opening of cracks in upper layers in response to a weak compressional regime. However, the structure is best explained by the effect of bedrock weathering that was primarily driven by climate and topographic control of reactive water flow, with regional compression playing a secondary role.

1. Introduction

Processes that transform bedrock into the porous regolith include fracturing, dissolution, precipitation, mechanical disaggregation, plant- and animal-related processes, and biogeochemical breakdown (e.g., Riebe et al., 2017). Regolith is important because it provides nutrients that support terrestrial life and porosity that stores groundwater (e.g., Graham et al., 2010; Riebe et al., 2017). Regolith is thinned by erosion, which physically removes material from the land surface, sometimes flattening and sometimes creating relief, shaping Earth's surface morphology and its Critical Zone (CZ) (Brantley et al., 2007). Recently, a few models have been presented that explain how the thickness of regolith responds to long-term changes in tectonics and climate (e.g., Dunne, 1990; Riebe et al., 2017; West, 2012).

But much remains unknown about coupling between physical, chemical, and biological processes within the CZ. Several hypotheses have been proposed to describe how key components of the CZ, such as groundwater flow (e.g., Brantley et al., 2017; Rempe & Dietrich, 2014), geochemical reactions (e.g., Lebedeva & Brantley, 2013), climate (e.g., Anderson et al., 2013), and topography coupled to tectonics (e.g., St. Clair et al., 2015) influence bedrock weathering and regolith thickness. A key goal is to understand coupling between the land surface, the depth of mobile soil, and the depth to mineral reaction fronts such as those that control bedrock to regolith transformations (Lebedeva & Brantley, 2020; Rempe & Dietrich, 2014).

Many of these emerging models (e.g., Anderson et al., 2013; St. Clair et al., 2015) emphasize the importance of physical processes such as fracturing (Eppes & Keanini, 2017) in controlling regolith. For example, some have proposed the opening of fractures in response to tectonic and topographic stresses (e.g., St. Clair et al., 2015) while others emphasize the freeze-thaw fracturing processes that are driven by regional climate patterns during segregation ice growth (e.g., Anderson et al., 2013). The effect of frost-cracking can propagate to relatively deep depths depending upon climate (Anderson et al., 2013). Another set of models emphasizes the importance of meteoric water flows and their associated influences on dissolution and precipitation reactions (Anderson et al., 2019). If reactions occur and the dissolved products are transported away through advective or diffusive transport, chemical weathering can create or destroy subsurface porosity (e.g., Brantley & White, 2009). One such flow and reaction model predicts thick regolith under ridgelines that thins toward valleys (Brantley & Lebedeva, 2020). Similar predictions arise from another hydrologically focused hypothesis that suggests the strongest control on the depth to unweathered material is the rate that equilibrated water is drained out of a weathering landscape by stream incision at the valley (Rempe & Dietrich, 2014). Models have also been proposed combining these two approaches (e.g., Harman & Cosans, 2019).

One way of evaluating these hypotheses is to use geophysical methods to map regolith for comparison to model predictions. Geophysical methods have been used successfully to image CZ structure at length scales ranging from centimeters to kilometers (Parsekian et al., 2015). Specifically, seismic velocities, which are a physical property related to the density and elastic moduli of Earth materials, have been used as a proxy to delineate the interfaces that separate soil, saprolite, weathered bedrock, and fresh crystalline bedrock (e.g., Befus et al., 2011; Flinchum et al., 2018; Holbrook et al., 2014). Seismic velocities have also been used to estimate porosity, fracture density, water content, mineralogy, and textural characteristics (e.g., Flinchum et al., 2018; Gu, Mavko, et al., 2020; Holbrook et al., 2014; Ma et al., 2021). However, most seismic models of the CZ are 2D models, and thus provide limited constraints spatially on the subsurface CZ structure. To date, 3D seismic images of CZ structure are available for only a few localities (e.g., Keifer et al., 2019; Wang et al., 2019, 2020).

Here, we evaluate aspects of the hypotheses described above using a 3D Vp image of the subsurface of an east-west oriented watershed developed on shale located in the Susquehanna Shale Hills Critical Zone Observatory (SSHO) in central Pennsylvania, USA (Figure 1). By combining the 3D seismic velocity structure of the Shale Hills watershed with well logs, geochemical data, a stress model, and hydrological observations, we document the importance of climate and topographically driven water flow and chemical reactions in driving development of the subsurface structure of the CZ.

2. Background

Our study site is a V-shaped forested subcatchment (0.08 km^2) developed mostly on Rose Hill shale, with a small portion over Keefer sandstone (Brantley et al., 2018; Sullivan et al., 2016) (Figure 1). Interbedded sandy and calcareous shale layers occur especially towards the Keefer contact (Sullivan et al., 2016). The average dip of shale bedding is 64° as observed in soil pits in the northern and eastern parts of the catchment, but can vary from 40° to 88°. Downhole televiewer images from boreholes near the outlet show almost flat-lying beds (Sullivan et al., 2016). Some variations may be caused by small folds as observed in nearby outcrops (Brantley et al., 2018; Sullivan et al., 2016).

Today's climate at Shale Hills is humid with a mean annual air temperature of 10°C and precipitation of 1,070 mm (Brantley et al., 2018). During the past ~2 Ma, the catchment experienced a periglacial climate with repeated glaciations (Clark & Ciolkosz, 1988) including the most recent Last Glacial Maximum (LGM) ~15 kyr ago. The poorly stratified and variable thickness colluvial sediments in the valley floor are consistent with periglacial deposits commonly found throughout the Valley and Ridge of central Pennsylvania (Clark & Ciolkosz, 1988).

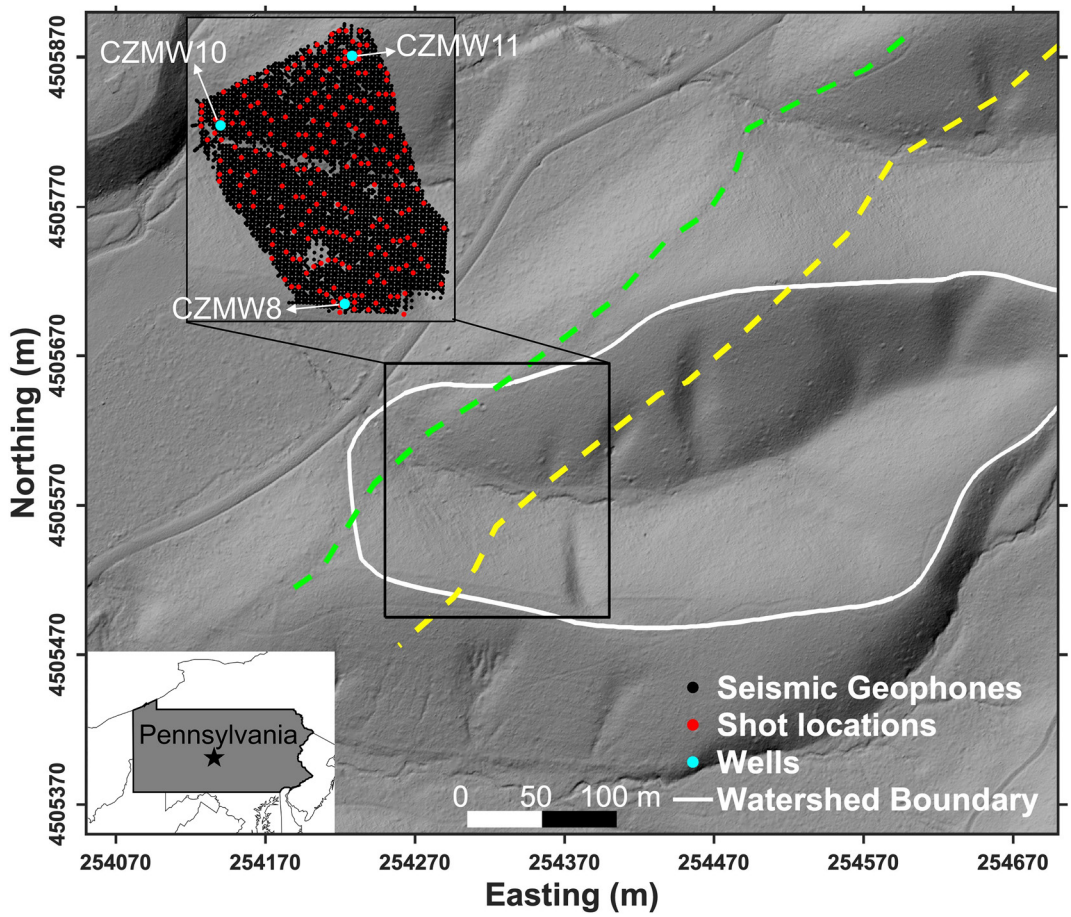

Figure 1. Map of Shale Hills catchment showing locations of seismic geophones, seismic shots, and boreholes used in the study. Background is the shaded relief map from a LIDAR DEM image. The coordinate system is the Universal Transverse Mercator system in zone 18N. Green dash line is the contact between the Keefer sandstone to the northwest and Rose Hill shale to the southeast (from Sullivan et al., 2016). Above the yellow dash line, interbedded sandstone layers are more frequently present (Sullivan et al., 2016).

The catchment is divided into N and S hillslopes by an ephemeral, west-flowing stream (Figure 1). The relief of each hillslope is ~30 m and the slopes range from 8° to 30°, with N-facing slopes 5°–10° steeper than S-facing (West et al., 2014). In general, augerable soil, thin near the ridgetops (~30 cm), thickens downslope toward the valley, where the soil + alluvium attains thicknesses of ~3 m in some locations (Jin et al., 2010; Lin et al., 2006). Beneath augerable soil in the lower hillslopes, variable amounts of colluvium and/or rubbly shale (both of which are impenetrable to augering) are present. The lower reaches of the N-facing slopes are mantled by thicker soil and colluvium than S-facing slopes (West et al., 2013). Although most of the hillslopes are sub-planar, infrequent gullies, referred to here as swales, occasionally punctuate the slopes. These swales, more frequent on the S-facing slope (Figure 1), collect thicker soil compared to the nearby sub-planar slopes (Jin & Brantley, 2011; Lin et al., 2006).

The subsurface structure of Shale Hills has been investigated in several previous studies using 2D P-wave velocity profiles together with geochemical and other data (Gu, Mavko, et al., 2020; Ma et al., 2021; West et al., 2019). Four layers were identified in these studies, with the shallowest layer ($300 < Vp < 600$ m/s) attributed to mobile soil, a layer with $600 < Vp < 2{,}700$ m/s attributed to chlorite-altered shale and a layer with $2{,}700 < Vp < 4{,}000$ m/s attributed to trace-weathered shale. The deepest layer with Vp of ~4,000–4,500 m/s was attributed to unweathered shale bedrock. To characterize the shallowest layer, West et al. (2019) compared several seismic velocity profiles to soil pits (Lin et al., 2006) and noticed that a Vp of 600 m/s defined the bottom of the (dry) mobile soil layer, especially along hillslopes. West et al. (2019) attributed this layer to augerable disaggregated soil. Below this mobile soil layer, Gu, Mavko et al. (2020), Gu, Rempe et al. (2020) argued that the first major growth of

porosity in the shale occurs at depths where chlorite begins to dissolve in the shale, and deeper than that, the shale is characterized only by trace weathering of the low-abundance minerals pyrite and carbonate as measured from geochemical samples. The onset of chlorite dissolution was found to correspond to Vp = 2,700 ± 200 m/s (Gu, Mavko, et al., 2020). This correspondence was observed from a 2D seismic transect that intersected two boreholes (CZMW8 on south ridge and CZMW10 under the valley near the outlet, Figure 1). Televiewer images from these boreholes did not show consistent changes in fracture densities at the depths of this contour, so the change in Vp was not attributed to fracturing (Gu, Mavko, et al., 2020). By comparing velocity profiles, sonic log data, and the geochemistry of borehole chip samples, Gu, Mavko et al. (2020) and Ma et al. (2021) showed that the Vp of the unweathered shale is ∼4,000–4,500 m/s.

3. Data and Methods

3.1. 3D Seismic Experiment

We collected a seismic refraction data set for 3D imaging using >4,000 geophones spaced 2 m apart over the western one-third of the Shale Hills watershed (Figure 1). The seismic data, recorded at a 2-ms sampling rate, have a 20–200 Hz frequency range with a dominant frequency of ∼50 Hz (Figures 2a and 2b). We filtered the raw seismic data using a 4-th order wide bandpass filter with corner frequencies at 20 and 100 Hz to suppress high-frequency noise (Figure 2a). We utilized a semiautomatic picking workflow (Figure S1 in Supporting Information S1), validated against about 18,000 handpicked arrival times (Figure S2 in Supporting Information S1), to obtain P-wave arrival times from seismic shots with relatively high signal-to-noise ratio. A total of about 160,000 first arrivals were obtained from 211 evenly distributed shots, resulting in uniform data coverage (Figure 2e). The root mean square (rms) value of all reciprocal source-receiver pick differences is ∼3.5 ms (Figure 2c). About 50% of the total reciprocal pairs are within 3 ms and 72% are within 5 ms. The maximum source-receiver offset is ∼150 m (Figure 2d); however, only 8% of picks came from source-receiver pairs with offset >100 m because data quality was limited at larger offsets. A few 2D transects extracted from the data set have been modeled previously, as discussed above (Gu, Mavko, et al., 2020; Ma et al., 2021). Additional details about the data collection and workflow are provided in the Supporting Information S1, and Ma et al. (2021) also provides details about the data collection.

3.2. Wave-Equation Travel-Time Tomography (WTT)

We employed WTT to image the subsurface Vp structure using the P-wave arrival times. The conventional ray-theoretic travel-time (RTT) method has been used to image Critical Zone structures in many studies, including for Shale Hills (e.g., Befus et al., 2011; Flinchum et al., 2018; Gu, Mavko, et al., 2020; Holbrook et al., 2014; Ma et al., 2021; St. Clair et al., 2015; West et al., 2019). The RTT computes travel time using geometric ray theory, which is a high-frequency approximation of the wave equation. In WTT, travel time is derived from a seismogram by solving the wave equation. Both early theoretical studies (e.g., Luo & Schuster, 1991; Williamson, 1991) and recent tomography results (e.g., Fu & Hanafy, 2017) have shown that WTT is capable to provide more accurate and higher resolution P-velocity images compared to RTT. Our wave-equation solver, based on the discontinuous-Galerkin method (Dumbser & Käser, 2006; Käser & Dumbser, 2006), achieves high-order accuracy in both space and time on 3D unstructured tetrahedral meshes. The source we used for wave simulation was a vertical Dirac pulse, and the synthetic seismic data generated by the WTT method were filtered using the same bandpass filter applied to the data.

The tetrahedral mesh used in our study is displayed in Figure S3a in Supporting Information S1. The free surface of the mesh conforms to the land surface obtained from LIDAR digital elevation map (DEM) (Figure 1). The required minimum element size of our mesh is determined by the minimum wavelength, which can be estimated from the Vp structure of the study area. The seismic velocities at shallow depth are much slower than at deeper depths (Gu, Mavko, et al., 2020; Ma et al., 2021; West et al., 2019). Thus, seismic waves, for a given frequency, have much shorter wavelengths at shallow depths compared to deeper depths. Given this, to maximize computing efficiency while retaining computing accuracy, the element size of our mesh was increased from 1 m at the surface to 10 m at the bottom of the model, with an even coarser mesh outside our survey area (Figure S3a in Supporting Information S1).

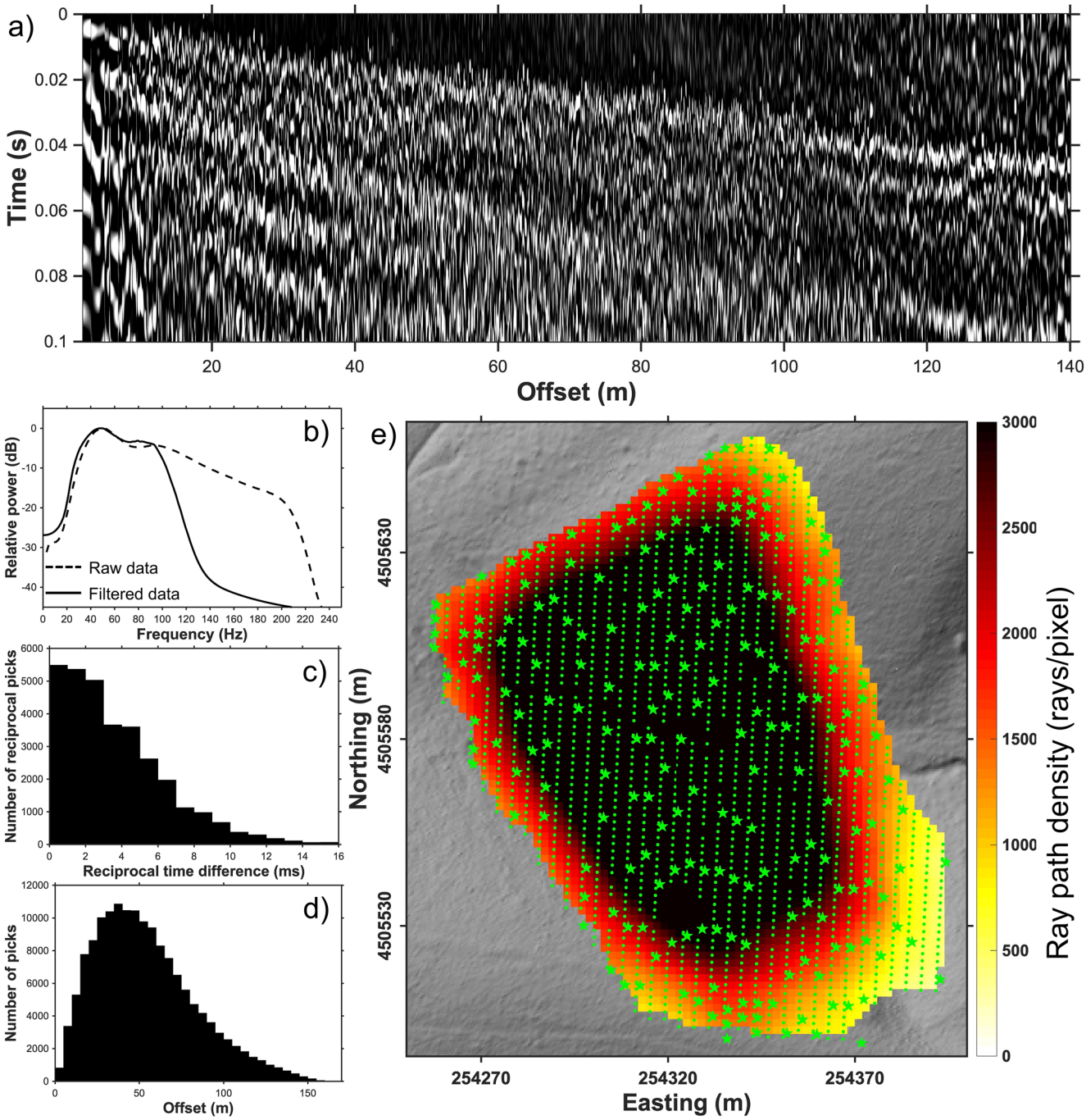

Figure 2. (a) An example of a seismic shot gather after filtering plotted in source-receiver offset. (b) Frequency spectrum for a raw and filtered shot gather. (c) Histogram of number of shot-receiver pairs versus reciprocal time difference. (d) Histogram of number of first arrival picks versus source-receiver offset. (e) source-receiver path density. Green stars are selected shots with good data quality and the green dots are location of the geophones in Figure 1.

WTT is in essence a gradient-based iterative numerical optimization algorithm, in which we search for an optimal Vp model that can minimize an objective function defined in terms of the differences between observed and model-predicted travel times. The gradient (i.e., sensitivity kernel) of our objective function was calculated using the adjoint method (e.g., Fichtner et al., 2009; Lee et al., 2014; Tape et al., 2009; Tarantola, 1988; Tromp et al., 2005; Wang et al., 2019, 2020) and back-propagated to improve the Vp model by reducing the travel-time misfits. Two adjoint kernel examples are shown in Figures S3b–S3e in Supporting Information S1. Conceptually, the adjoint kernels (perturbation of travel times with respect to velocity) tell us how to change our Vp model in

order to reduce the travel-time misfit. In (b) and (d), the travel-time misfit is negative (i.e., synthetic arrival time larger than observed arrival time) and the kernel is positive (warm color), indicating the velocity model is too slow along the source-receiver path. In contrast, in (c) and (e), the travel-time misfit is positive (i.e., synthetic arrival time smaller than observed arrival time) and the kernel is negative (cold color), indicating the velocity model is too fast along the source-receiver path.

To initiate the iterative algorithm for optimization, a 1D starting (initial) P wave velocity model was developed using borehole information and the previous 2D P wave velocity studies described in Section 2 (Gu, Mavko, et al., 2020; Ma et al., 2021; West et al., 2019). Velocities were fixed at 300 m/s at the surface and 4,500 m/s at some depth. Then, a grid search to minimize travel-time misfit was used to determine an optimal gradient between those values (i.e., 300 and 4,500 m/s). Using the 1D starting model obtained (Figure S4a in Supporting Information S1), 12 iterations of the WTT optimization algorithm were performed, achieving a reduction in the rms travel-time misfit from 6 to 3.5 ms (Figure S4a in Supporting Information S1). A 3.5 ms misfit is similar to the uncertainty of the travel-time picks. The reduction achieved in the scatter of travel-time residuals with offset between the starting 1D model and the final 3D model is illustrated in Figures S4b and S4c in Supporting Information S1.

4. Model Results and Subsurface Layering

To estimate the resolution, we carried out checkerboard tests using the Gauss-Newton approximate Hessian of the last iteration (e.g., Lee et al., 2014; Wang et al., 2019, 2020). A synthetic checkboard model with positive and negative velocity perturbation of 20% was used. The horizontal dimension of the input checkers was set to 15 m. The vertical dimension for checkers in the topmost layer was set to 5 m and below that 10 m. Recovered checkerboards are shown in map view at various depths and cross-sections in Figure 3. Regions with clearer recovered checker pattern (i.e., shape and amplitude) illustrate where the resolution of the model is highest. Each individual checker can still be identified to ∼20 mbls (meters below land surface) (Figure 3). Beyond 20 m depth, boundaries between checkers blur and the resolution deteriorates, especially close to the edges of the model (Figure 3). The results of the checkerboard resolution test illustrate that our 3D Vp model can be resolved to ∼20 mbls in the center of the model and to ∼15 mbls toward the margins of the model.

We show map views of the 3D seismic model at depths from 1-20 mbls in Figure 4 and provide a 3D movie in the Supporting Information S1. To attribute geological significance to the depth-dependent velocity changes, we follow the interpretation used by West et al. (2019), Gu, Mavko et al. (2020), and Ma et al. (2021), reviewed in Section 2. Specifically, the shallowest layers ($300 < Vp < 600$ m/s) are referred to as mobile soil (noting it may include some alluvium and/or colluvium), layers with $600 < Vp < 2{,}700$ m/s are referred to as chlorite-altered shale (noting it could include colluvium), and layers with $2{,}700 < Vp < 4{,}000$ m/s are referred to as trace-weathered shale. In samples from these latter depths, we typically only detect pyrite oxidation, carbonate weathering, and fractures. The deepest layer is attributed to unweathered bedrock where values of Vp are ∼4,000–4,500 m/s.

4.1. Depth of Mobile Soil (Vp = 600 m/s)

Using a value of $Vp = 600$ m/s to estimate the depth of mobile soil yields an estimate for mobile soil that is generally <0.5 m along S-facing sub-planar hillslopes (Figure 5a). In contrast, on the N-facing sub-planar hillslopes, the regolith thickness is highly variable, ranging from 0 to ∼1.3 m (Figure 5a) and to as deep as 2 m under the swale on that slope. These values for mobile soil on hillslopes are all roughly consistent with field observations, as described in previous publications (e.g., Jin et al., 2010; Lin et al., 2006).

However, along the valley floor, we observed discrepancies in depths of field-observed mobile soil (+alluvium) when we predicted it using the value of $Vp = 600$ m/s. For example, this Vp leads to the inference of almost zero mobile soil + alluvium thickness along parts of the valley floor (Figure 5a) even though augering has shown the thickness is as deep as 3 m in several points along the valley floor (Lin et al., 2006; West et al., 2014). We hypothesized this discrepancy is caused by water saturation along the valley floor during the wet month of our seismic experiment because seismic velocities of soil and sediment are much higher when water-saturated as opposed to air-saturated (e.g., Nur & Simmons, 1969). The seismic velocities in the mobile soil are especially affected by water saturation in the valley because the water table depth varies temporally from above the land surface (snowmelt

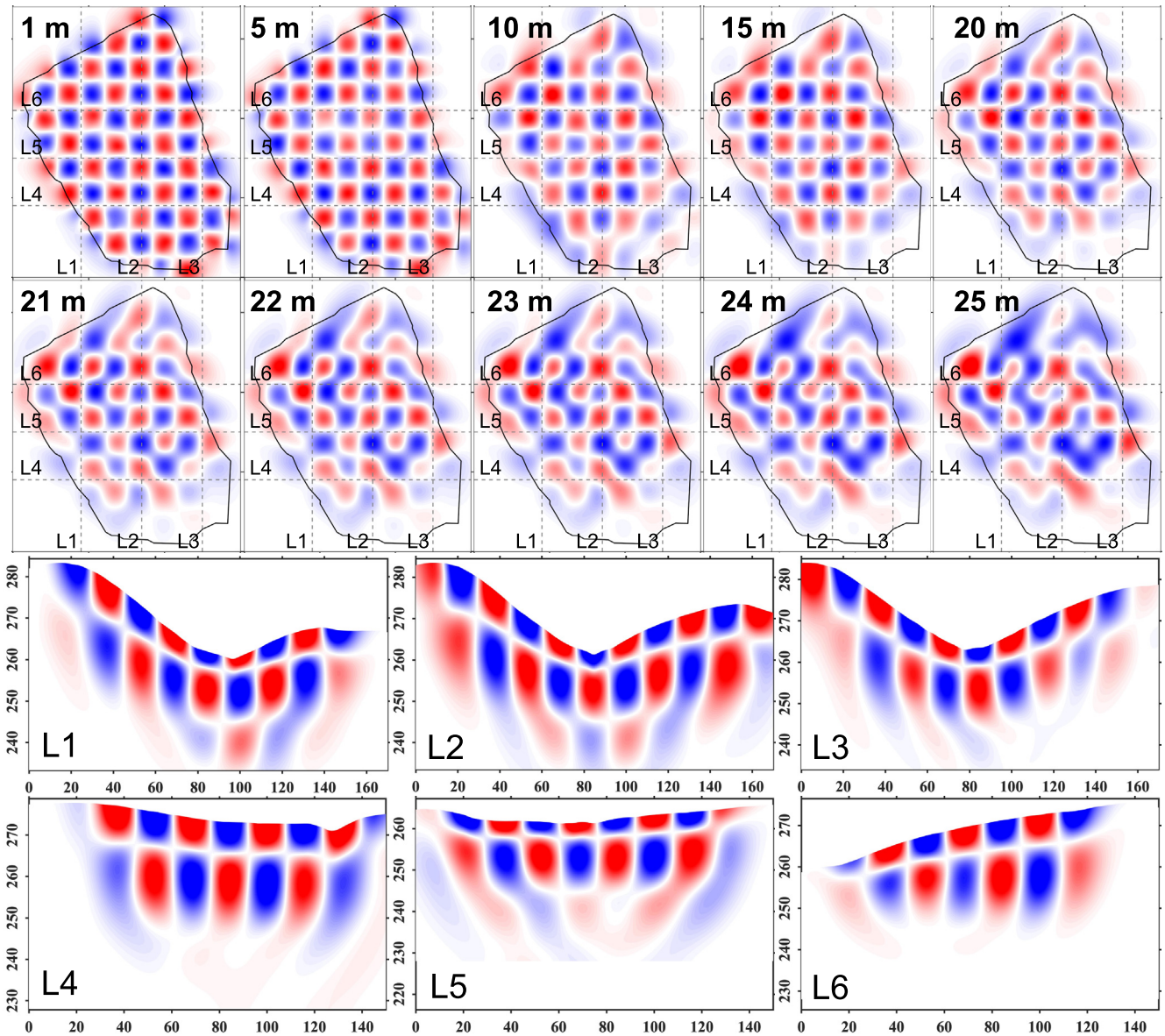

Figure 3. Resolution test results. The input checkers are 15 m in the horizontal direction. In the vertical dimension, the thickness of checkers on top layer is 5 m and the thickness of checkers below is 10 m. Top panels: Map-view plots of checkerboard tests at 1, 5, 10, 15, 20, and 21–25 mbls as indicated in the upper left corner of each panel. Labeled black dash lines show locations of the six cross sections in the bottom panels. The vertical axis of cross-sections is exaggerated by two times.

to early summer) to 1–2 mbls (approximately July through April) in the channel (it varies from ~18 to 25 mbls under the ridge crests) (Sullivan et al., 2016).

To explore this hypothesis, we assumed 30% porosity (Gu, Mavko, et al., 2020; Lin et al., 2006) and used the rock-physics model presented in Gu, Mavko et al. (2020) for Shale Hills to predict the mobile soil thickness (Figures 5b and 5c) from the seismic velocities based on different saturation assumptions, that is, 100% gas- and 100% water-filled material. The 100% gas-filled model predicts thin mobile soil thicknesses throughout much of the study area (Figure 5b) that differ substantially from thicknesses observed in the field along the valley floor (Figure 5a). The 100% water-filled porosity model predicted a more reasonable mobile soil thickness along the valley floor (Figure 5c). Our seismic model thus yields mobile soil thicknesses that are consistent with field observations (and with the work of West et al., 2019), but only if the varying degree of water saturation in valley bottom and hillslopes is incorporated.

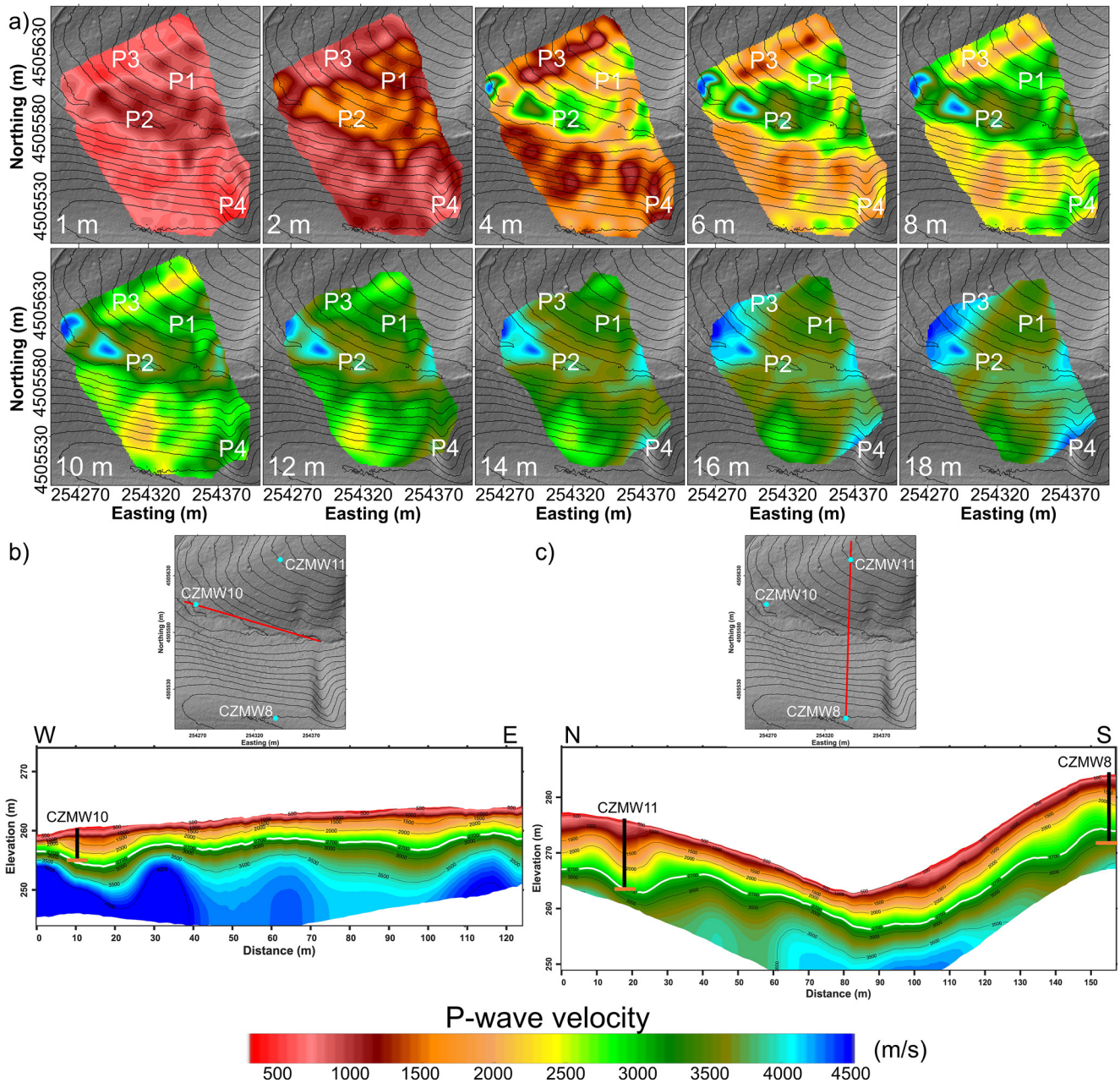

Figure 4. (a) Map view plots of the 3D Vp model results plotted at depths varying from 1–18 mbls as indicated in lower left corner of each panel. Areas close to the data array boundary with limited resolution are masked out. P1-4 are markers reference in the text to highlight important features of the model. (b) 2D transect of 3D Vp along the valley floor extracted from the 3D model. (c) 2D transect of 3D Vp across the valley floor extracted from the 3D model. The red solid lines on the LIDAR hillshade map show the locations of the 2D transects. The white contour in the 2D Vp transects shows the Vp of 2,700 m/s, which corresponds to the onset of the chlorite dissolution front. Orange horizon lines at the bottom of black vertical lines indicate the geochemically measured depth of initiation of chlorite dissolution (Table S1 in Supporting Information S1).

4.2. Depth of Chlorite-Weathered Shale (Vp = 2,700 m/s)

Next, we examine deeper Vp variations, focusing on the contour of Vp = 2,700 m/s that has been attributed to the major onset of growth of porosity in the shale as chlorite weathers (Gu, Mavko, et al., 2020). We retested the hypothesis that chlorite begins to weather at Vp = 2,700 m/s from Gu, Mavko et al. (2020) for additional boreholes (Figure 6) by extracting the P-wave velocities from our 3D Vp model at each well where chlorite dissolution was noted from geochemical measurements on core material (Table S1 in Supporting Information S1). The Vp at the

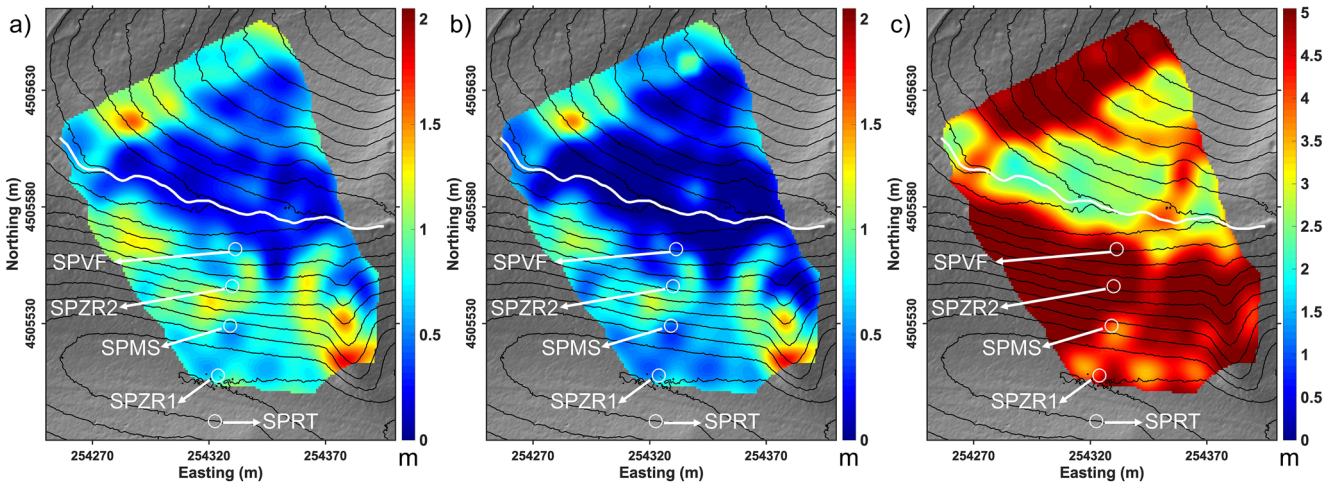

Figure 5. Mobile regolith thickness in meters (a) using Vp of 600 m/s from the seismic model, (b) predicted using a porosity of 30% assuming 100% gas-filled pores, and (c) predicted using a porosity of 30% and 100% water-filled pore. White circles are locations of soil pits with soil thickness predictions. The predicted soil thickness is given next to the name of each soil pit. The measured (known) thickness for each pit is as follows: SPVF (0.67 m), SPZR2(0.59 m), SPMS (0.59 cm), and SPZR1 (22 cm). At some points along the channel (white line), the soil thickness was measured to be as deep as 3 m (Lin et al., 2006; West et al., 2014).

inferred onset of chlorite dissolution determined geochemically from the wells ranges from ~2,400 to 3,300 m/s with an average value of 2,840 ± 340 m/s (Table S1 in Supporting Information S1), consistent with the published estimate (2,700 m/s ± 200 m/s). The largest discrepancy was found at CZMW8, located within 1.5 m of the model boundary (Table S1 in Supporting Information S1) where model resolution degrades (Figure 3). If we ignore CZMW8, the average value for onset of chlorite dissolution is 2,686 ± 228 m/s, within the error of 2,700 m/s (Gu, Mavko, et al., 2020; Ma et al., 2021).

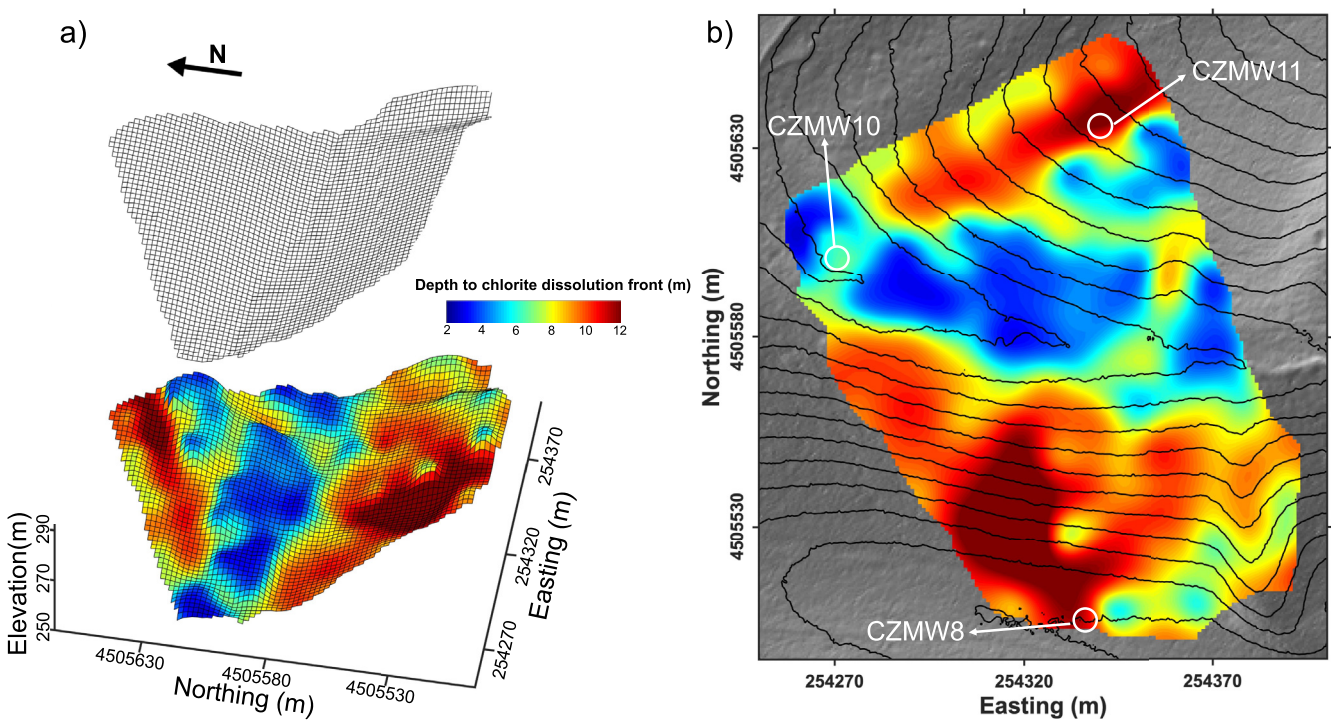

Figure 6. (a) 3D perspective view and (b) 2D map view of the chlorite dissolution front colored by depth to onset of chlorite dissolution. The gray grid of land surface is shifted up 100 m for a better visualization of both land and weathering front surfaces. The elevation of the onset of chlorite dissolution was extracted from the seismic model using Vp of 2,700 m/s. The depth (b) to onset of chlorite dissolution was calculated subtracting the chlorite dissolution front elevation from the land surface elevation. White circles are locations of the three boreholes shown in Figure 1.

4.3. Depth to Unweathered Bedrock

Because well-resolved seismic structures in the 3D model are restricted to ~20 mbls, the depth of trace-weathered shale is only observed in some regions of the catchment. Nonetheless, the topography of the depth to bedrock, inferred from Vp ≈ 4,000 m/s, changes sharply in one location, namely along the north ridge near the outlet where lower seismic velocities are observed beneath the northwest side of marker P3 in Figure 4. This is the only area of the catchment not underlain by Rose Hill shale. Sandy and limey layers are more frequent near the contact between shale and Keefer sandstone (Figure 1). The orientation of this velocity boundary is approximately parallel to the contact of the Keefer sandstone and the Rose Hill shale. The reduction in seismic velocity in this area is therefore attributed to the increase of carbonate-rich and sandy interlayers as the shale formation grades to sandstone.

4.4. Roughness and Topography of Weathering Interfaces

From Figures 4 and 6, we can make some broad observations about the roughness and topography of the subsurface reaction landscapes (interfaces marking initiation of weathering reactions). We focus on the interfaces between (a) mobile soil and chlorite-altered shale, and (b) chlorite-weathered and trace-weathered shale. Roughness is considered at the scale of resolution of the seismic model (~15 meters).

First, the interfaces defined by Vp = 600 m/s (bottom of mobile soil) and 2,700 m/s (onset of chlorite dissolution) are generally rougher than the surficial landscape (Figures 4 and 6). The mesh plot in Figure 4a reveals that interface marking the onset of chlorite dissolution (the chlorite weathering front) shows more variations as compared to the surficial landscape.

A second important observation is that the contour for Vp ≈ 600 m/s is deeper beneath the N-facing than S-facing slopes (marker P1 in Figure 4), that is, the mobile soil is thicker on sub-planar hillslopes on the shadier side of the catchment. Vp values are also faster beneath the valley (marker P2 in Figure 4) than under the hillslopes at comparable depths below land surface, that is, the subsurface landscapes delineating the bottom of mobile soil and chlorite alteration are shallower under the valley than hillslopes.

Finally, we also observe that beneath the one swale within our study area, velocities are slower at shallower depths (1–8 mbls) but faster at larger depths (below 8 mbls) compared to the adjacent sub-planar regions of hillslope (marker P4 in Figure 4). This means that the depth of mobile soil is thicker in swales, as previously noted (Lin et al., 2006), but that the depth of the interface between chlorite-weathered and trace-weathered shale rises closer to the land surface under the swale.

5. Discussion

We now examine the spatial variations in our 3D model, focusing on the contours for 600 (depth of mobile soil), 2,700 (depth of chlorite-altered shale), and 4,000 m/s (depth of unweathered bedrock), together with information from geochemistry, hydrology, and fracturing to explore the hypothesized weathering mechanisms mentioned in the introduction, namely topographic stress-induced fracturing (St. Clair et al., 2015), climate-driven fracturing (Anderson et al., 2013; West et al., 2019), and a coupled hydrogeochemical flow and reaction (Brantley & Lebedeva, 2020; Rempe & Dietrich, 2014).

To test the stress-induced fracturing mechanism, we calculated a 3D stress model and the failure potential, FP, as a function of depth and position using the same approach as St. Clair et al. (2015). Additional information is summarized in the Supporting Information S1 and Ma et al. (2021). FP is a dimensionless proxy that represents the likelihood of generating and reactivating shear fractures (Iverson & Reid, 1992). FP, calculated as the ratio between maximum shear and mean normal stress, varies from 0 (low likelihood of fracture opening) to 1 (high likelihood of fracture opening). We cannot determine whether a fracture opens at any depth from a given value of FP because fracture opening in near surface environments is a complex function of fracture orientations and characteristics, porewater saturation, fluid reactivity, rock composition, and texture (Eppes & Keanini, 2017). We therefore consider only arbitrary values of FP and their relative magnitude variations. For reference, a recent study by Moon et al. (2020) analyzed ~50,000 fractures from granitic rocks, over a depth range of 600–0 m in Sweden. A comparison between the actual fracture openness and shear failure proxy on fracture planes showed that fractures with FP > 0.4 were likely to be open.

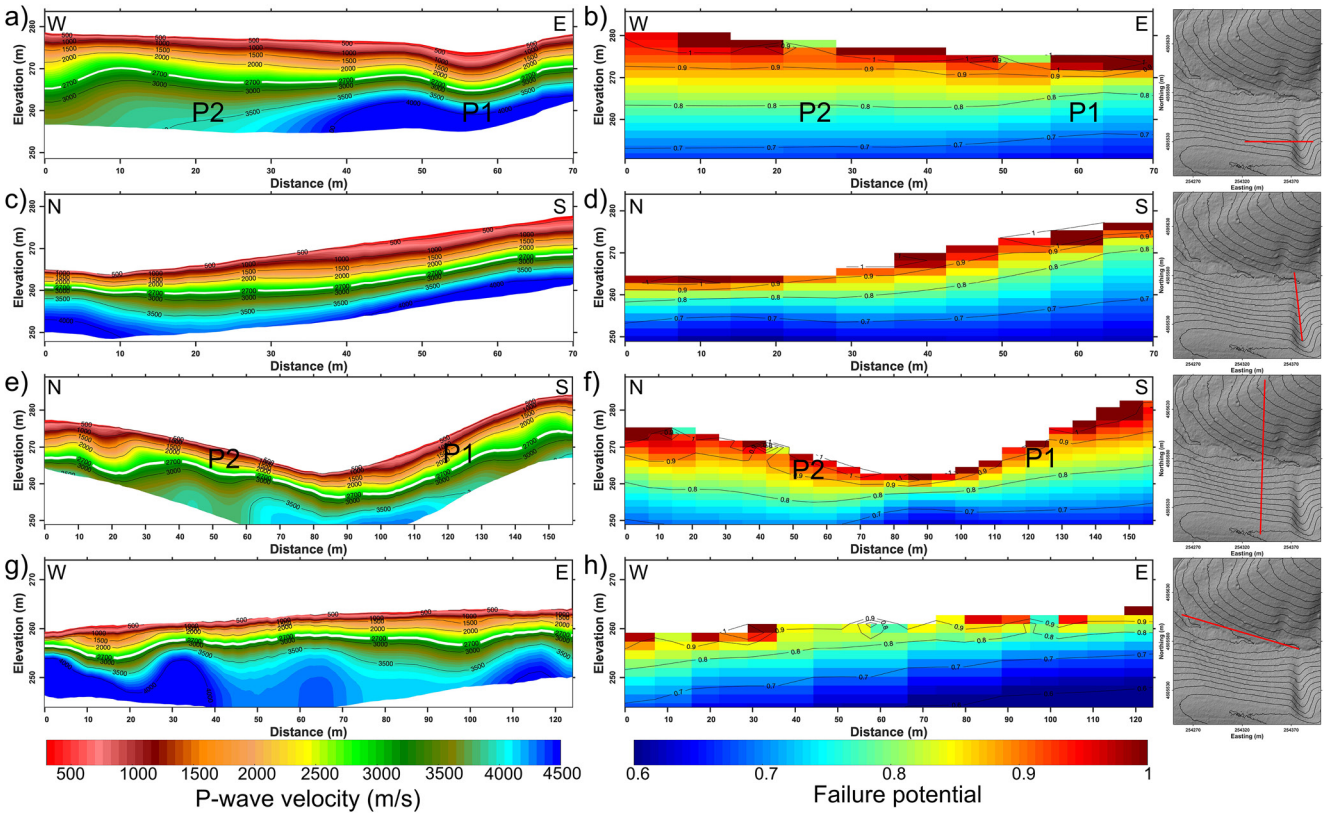

Figure 7. 2D transects extracted from the 3D Vp model (left panel) and failure potential (right panel) calculated from the 3D stress field under weak compression scenario cross swale (a), (b), along swale (c), (d), cross valley (e), (f), and along valley (g), (h). P1-2 in (a), (b), (e), and (f) are markers used to highlight model features mentioned in the discussion section. The white line in the 2D Vp transects is the Vp of 2,700 m/s, which corresponds to the onset of the chlorite dissolution front. The red solid lines on the LIDAR hillshade map show the locations of the 2D transects.

Ma et al. (2021) showed that for the stress model to account for variations in P-wave velocities along two profiles extending across the Shale Hills watershed and into neighboring catchments, the compressive stresses in this region of the Valley and Ridge must be weak. Therefore, here we consider the results for only the scenario with a weak horizontal compression, and for each subsurface interface, we discuss each of the proposed models of weathering.

5.1. Controls on Depths of Mobile Soil

Our 3D seismic velocity model reveals an aspect-related asymmetric pattern of depth of mobile soil (Vp $\leq \sim$ 600 m/s) (Figures 4, 7, and S5a in Supporting Information S1). This asymmetry was previously noted by West et al. (2019) using multiple 2D seismic transects along N and S slopes at Shale Hills. They showed that aspect-dependent microclimates during periglacial climates—such as experienced at Shale Hills during the LGM—can explain the asymmetries in depths of regolith and in surficial topography. Specifically, their explanation suggests that frost-cracking under the shadier (N-facing) hillside extends to larger depths than under the sunnier (S-facing) hillside, but the frequency of frost-cracking events under the sunnier hillside is higher than under the shadier side. The asymmetry in depth of cracking was invoked to explain deeper regolith on the N-facing side of the catchment, while the lower cracking frequency on the N-facing side was invoked to explain why the erosional efficiency of the N-facing side is lower (West et al., 2013). The lower erosional efficiency of the N-facing side in turn explains why the N-facing hillside steepened over geological time and why colluvium is retained to a greater extent at the base of the N-facing as opposed to the S-facing hillslope. These observations thus support the climate-driven frost-cracking hypothesis as an important mechanism in explaining depths of mobile soil as well as why N-facing slopes are steeper than the S-facing slopes. This latter asymmetry is also observed in other similarly oriented valleys in the Valley and Ridge physiographic province in the northern hemisphere (West et al., 2014).

We next test if, in addition to frost-cracking as a mechanism, the topography-coupled stress-driven fracturing model could also contribute to explaining mobile soil thickness. Figure 7 shows the mapped FP calculated for the catchment. This figure shows that the frost-cracking model is a better explanation for the asymmetric pattern of depth of mobile soil (Vp ~ ≤600 m/s) than topographic stress-induced fracturing (St. Clair et al., 2015). Specifically, the 3D stress model shows higher FP extending to deeper depths beneath the S-facing slope (marker P2 in Figure 7f) than the N-facing slope (marker P1 in Figure 7f). This prediction is opposite to the observed depths of mobile soil (600 m/s contour) (Figure 7e). Therefore, the topographic stress model is inconsistent with the observed mobile soil thickness.

A third explanation for the observed variations in mobile soil thickness is a hydrogeochemical flow and reaction model for regolith growth. Specifically, the extent or depth of geochemical reaction generally increases with the flux of water through weathering material (Brantley & Lebedeva, 2020) and more water fluxes through the soils on the N-facing than S-facing sides because the shady side loses less water to evapotranspiration (Sullivan et al., 2019). This hydrogeochemical model thus can contribute to explaining why the N-facing soils are generally deeper than S-facing soils. In addition, this model can also explain why N-facing soils are more depleted in base cations and clays compared to the S-facing soils (Ma et al., 2013; Sullivan et al., 2019). Frost-cracking and hydrogeochemical weathering are thus viable explanations for the asymmetry in mobile soil depths on the two sides of the catchment, whereas the topographic stress model is not.

5.2. Controls on Depths of Chlorite-Weathered Shale

We now test if the topography and roughness of the interface defined by the 2,700 m/s contour can be explained by one or more of the three hypotheses. We first consider if frost-cracking could explain these aspects of the Vp = 2,700 m/s contour under the two types of hillslopes in the catchment (e.g., Brantley et al., 2018), namely sub-planar hillslopes and the concave-up valley and swales. Sub-planar slopes are locations where soil loss is largely diffusive in nature (e.g., Roering et al., 1999) while swales represent where channels initiate and remove soil advectively as well as diffusively (e.g., Perron et al., 2012). One relatively large swale is located on the N-facing hillslope (Figure 1).

To investigate concave-up land surface, Figure 7 was plotted to show the seismic transect (intervals of 5–12 m) that crosses the entire valley floor and one 2D transect along the valley axis. We similarly plotted three roughly parallel 2D transects along the N-facing hillslope crossing the swale at different positions sequentially from the ridgetop toward the valley and one 2D transect along the swale. In Figure 7, the highlighted white line is the 2,700 m/s contour, that is, inferred initiation of chlorite dissolution (and onset of porosity growth in shale matrix). The average depth 2,700 m/s contour is plotted by aspect in Figure S5b in Supporting Information S1.

We cannot test the frost-cracking hypothesis as a function of aspect for the swale because we only have one swale in the 3D model, so we only consider the frost-cracking model with respect to the valley versus hillside. Figure 7 shows that the contour for Vp = 2,700 m/s plots deeper under the N-facing slope (marker P1 in Figure 7e) than S-facing slope (marker P2 in Figure 7e). Frost-cracking has similarly been calculated to extend deeper under the N-facing as compared to the S-facing side of the catchment (West et al., 2019). We therefore conclude that climate-driven frost-cracking is a viable explanation for the subsurface pattern with respect to Vp = 2,700 m/s at P1 than P2.

We next test the tectonic-driven topography-coupled fracture model by again considering the stress model calculated for the transect that crosses the entire valley floor (Figure 7f). Broadly, the patterns in Vp mimic those of the weak stress model, suggesting that fractures open to shallower depths under the valley than under the ridges. For example, the depth to Vp = 2,700 m/s is shallower along the valley floor as compared to under the planar hillslopes (Figure 7g). At the same time, along the axis of the valley floor, the depth to 2,700 m/s is almost constant, ranging from 2-6 m (Figure 7g). Likewise, the depth to an arbitrary value of the FP is also shallower under the valley than under the hillslopes (Figure 7e) and the depth to an arbitrary value of the FP along the valley floor is similarly constant (Figure 7h).

Broad agreement is also observed between the patterns of Vp and FP under the swale. The seismic transects in Figure 7 show that even though the depth of mobile soil in the swale is thicker than on nearby planar hillslopes (presumably because of convergent advection of water and soil into the swale), the depth to Vp = 2,700 m/s is shallower under the swale (marker P2 in Figure 7a) than under adjacent planar hillslopes (marker P2 in Figure 7a).

Figure 7c also shows that along the swale from ridgetop to channel, the depth to Vp = 2,700 m/s is almost constant. Similarly, the depth calculated to FP = 0.8 is shallower (marker P2 in Figure 7a) than similar depths under the nearby planar hillslopes (marker P2 in Figure 7a). Likewise, along the axis of the swale from ridgetop to channel, the depth calculated to FP = 0.8 is almost constant (Figure 7d). Thus, at the same depth below the land surface, the FP is larger under the planar hillslopes as compared to under the swale, consistent with the potential for fractures to open to greater depths under the planar hillslopes compared to the swale. Such patterns could contribute to the patterns in Vp.

However, despite the broad agreement of Vp and FP under the weak stress regime, the Vp models show some inconsistences with the FP maps. For example, abundant second-order heterogeneities, especially along the valley floor (Figure 7g), are not easily explained with the fracturing model. More significantly, the fracture model predicts potentially higher FP (and thus, deeper fracturing) under the S-facing slope (marker P2 in Figure 7f) than the N-facing slope (marker P1 in Figure 7f). This prediction contradicts our observation from the contour of Vp = 2,700 m/s that the depth of the contour is deeper under the N-facing (marker P1 in Figure 7e) than the S-facing slope (marker P2 in Figure 7e). Thus, frost-cracking explains the catchment-wide asymmetries in Vp of N- and S-facing hillslopes better than the topography-driven fracturing model.

Finally, the third model, hydrogeochemical flow and weathering, provides a viable explanation of the patterns in Vp under the valley shown in Figure 7. These patterns in Vp are consistent with a vertically downward advance rate for chlorite dissolution that is constant everywhere along the axis under the valley or swale but slower than under nearby planar hillslopes when considered at similar depths. Hydrogeological observations of the watershed have shown that most of the precipitation into the catchment is channeled to the valley in shallow subsurface pathways instead of flowing vertically to the deep subsurface under sub-planar hillslopes and that much of the precipitation onto hillslopes near the swales are channelized to the swales, flowing downslope to the valley (Liu & Lin, 2015). These flow patterns limit the downward infiltration (and weathering) under concave-up land surfaces and potentially explain the shallowness of the depth to Vp = 2,700 m/s under the valley and swale. This attribute of concave-up land surface is important because the strongest control on weathering advance is usually the availability of meteoric water (e.g., Brantley et al., 2013).

The somewhat-paradoxical picture that emerges is that the predominantly wet valley and swales starve the deep subsurface under their channels from receiving vertically infiltrating water as compared to the nearby hillsides because they tend to remain hydraulically connected and drained by the stream (e.g., Liu & Lin, 2015). An additional contributor to this removal of water from the downward infiltration path under concave-up features is tree density. Tree density is higher in the valley and swales (Brantley et al., 2018) and this promotes the loss of swale water to evapotranspiration.

Other factors that might affect weathering under concave-up land surface largely cannot explain the observations. For example, compared to the planar hillslopes, swales at Shale Hills have higher organic content (Andrews et al., 2011), biomass, and oxygen concentrations (Yesavage et al., 2012), all of which might affect weathering. But the sum of these factors would likely result in a higher concentration of organic acids, and this also promotes faster, rather than slower, weathering (Ganor et al., 2009). Thus, unlike the patterns of water flow, none of these other factors are consistent with slower weathering under swales.

Other observations can also be reconciled with the hydrogeochemical flow + reaction mechanism. For example, some of the second-order heterogeneities shown in Figure 7g that are difficult to explain with the frost-cracking or topographic-driven fracturing mechanisms could be explained by flowpath patterns along the valley floor. Specifically, in addition to water flowing downward along the hillslopes, borehole logs have shown that water also flows upward above 21 mbls at well CZMW10 in the valley floor (Gu et al., 2020a) and chemistry of valley floor soil porewaters yield evidence of mixing between hillslope and subsurface valley waters that could accompany such upwelling (Jin et al., 2011). We propose that the second-order heterogeneities in Figure 7g along the valley may indicate such upwelling points.

In summary, the patterns in Vp in the shallow subsurface of Shale Hills (~20 mbls) are most consistent with a vertical advance rate for chlorite dissolution that is constant everywhere along the axis under the valley and swale but that is slower than under nearby planar hillslopes. Comparisons between Vp, FP, and the potential for subsurface weathering as shown in Figure 7 suggest that the topography-driven fracturing mechanism may contribute to subsurface weathering to some degree (producing broad agreement between Vp and FP), but the details

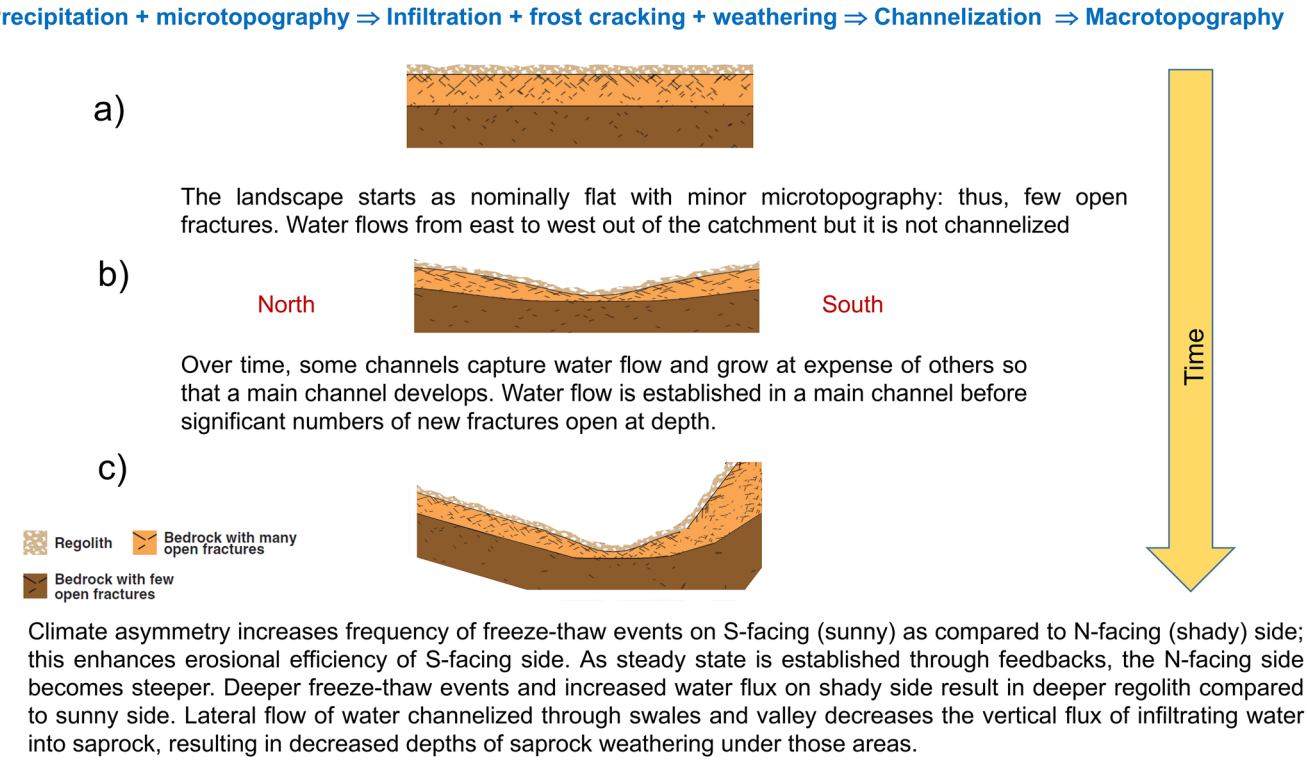

Figure 8. A schematic diagram showing how micro-climate effects result in asymmetries in surface slope and regolith depth at Shale Hills.

of shallow subsurface weathering patterns are best explained by climate- and topography-driven frost-cracking + water flow + biogeochemical reaction. Finally, structural variations in dip, folding, and lithology (Figure 1) are important for explaining small-scale variations in the buried interfaces of weathering. Such local geological heterogeneities explain why the subsurface weathering interfaces are rougher than the landscape surface (Figure 6), which is smoothed by downslope soil creep.

5.3. A Model for Catchment Evolution

The aspect-related micro-climate variation apparently plays a primary role in controlling the generally steeper and thicker depth of weathering under N-facing slopes at Shale Hills (both depth of mobile soil and depth to onset of chlorite dissolution). Shale Hills shows only limited influence from the weak compression experienced by the watershed and its associated topographically induced fractures (Ma et al., 2021). As discussed by Ma et al. (2021), the compressional regime may be weaker than inferred in other watersheds to the south (St. Clair et al., 2015) because of (a) the low strength of shale (i.e., its tendency to self-seal openings between bedding planes) or (b) its proximity to the glacial advance during the LGM (Ma et al., 2021). Regardless, the very low compressional stress regime is only a secondary influence on depths of weathering in the shallow subsurface (~20 mbls) at this location (it may be more influential at greater depths (e.g., Moon et al., 2020)).

Figure 8 shows a hypothetical, schematic diagram summarizing the development of the Shale Hills catchment. Based on the estimated erosion rate of 30 m/My (West et al., 2013) and an average relief of 30 m, the catchment has evolved for ~1 My. Positing a nominally flat hypothetical landscape with only micro-topography at time zero (Figure 8a), the potential for topography-driven fracture opening in the subsurface was minimal. However, very small undulations of the rough land surface would eventually have channelized water flow and advective transport of soil, allowing a channel to grow into a stream (Figure 8b). With channel growth, topography would also grow and the channel would have oriented east-west so as to cut through the highly resistant Keefer sandstone. Eventually, the subsurface FP from topographic stress would have become large enough to promote open subsurface fractures. Erosion was likely especially fast during periglacial periods, when frost-cracking events were frequent, affecting the erosional efficiencies of the catchment hillsides. In response to its lower erosional efficiency

(related to aspect), the N-facing side would have steepened as feedbacks drove the watershed toward a steady-state land surface geometry that could be roughly maintained over timescales of 1000s of years (Figure 8c). Throughout the periglacial periods during the last 1 My, the depth of frost-cracking under the shaded N-facing hillside remained greater than under the S-facing side, allowing deeper hydrogeochemically driven weathering of the subsurface under the more shaded side of the catchment. This climate-driven hydrogeochemical asymmetry can thus explain the asymmetry in erosional efficiency, hillslope, clay content, and base cation content (Sullivan et al., 2019; West et al., 2019).

6. Conclusion

We used data from an extraordinarily dense seismic deployment to image a 3D seismic structure of a small well-studied watershed to understand bedrock weathering. The three-dimensional seismic Vp model obtained from the data yielded sufficient resolution to image the subsurface landscapes of weathering to ~20 mbls. The mobile soil thickness predicted from seismic velocities are consistent with geochemical measurements from boreholes and observations from soil pits as long as the water saturation is included in the interpretation. We also mapped the depth to onset of chlorite dissolution under the watershed using the Vp of 2,700 m/s, a value shown previously (and corroborated here) that correlates with the onset of growth of porosity. The interface defined by this Vp contour is rougher than that of the land surface itself, an observation attributed to the heterogeneities in the deformed shale as well as smoothing of the land surface by diffusional soil processes. We found depths of weathering were deeper under N-facing as opposed to S-facing slopes and under planar hillslopes as compared to a swale and the valley bottom. Such patterns in weathering are best explained by a climate-driven model that invokes frost cracking and hydrogeochemical flow + reaction influenced by micro-topography (swales) and macro-topography (valley orientation). Concave-up channels starve the underlying subsurface from receiving vertically downward infiltration of water, slowing weathering below the channel axis. In addition, aspect-related differences in micro-climate on the N and S sides of the catchment explain differences in infiltration rates on each side. Our 3D Vp model broadly corresponds to the 3D stress field calculated for a weak stress regime, but the details of the Vp patterns (e.g., Vp = 600 m/s and 2,700 m/s) are explained better by topographic control on micro-climate and water flow. In this shale catchment, the effects of micro-climate and water flow are the primary controls on the depths to which weathering extends in the upper 20 meters of weathering, while opening of nonclimate-related fractures from the very low compressional stress regime provides a secondary influence.

Data Availability Statement

Seismic data are available from the IRIS Data Management Center and borehole logs from the Shale Hills CZO webpage (http://www.czo.psu.edu/data_geochemical_geophysical.html). Computational resources used in this study were provided by the NCAR-Wyoming Supercomputing Center.

Acknowledgments
Funding is acknowledged from DOE OBES DE-FG02-05ER15675 and NSF Critical Zone Observatory grants EAR 12-39285 and 13-31726 to Susan L. Brantley and NSF EAR 1945431 and 2012073 to Seulgi Moon Work at Shale Hills is facilitated by the Penn State College of Agricultural Sciences and Department of Ecosystem Science and Management as part of Penn State's Stone Valley Forest. We thank the IRIS Passcal Instrument Center for providing seismic equipment and logistical and data management support for this study, and we thank many contributors who helped with the seismic survey and Brad Carr who collaborated on borehole logs.

References

Anderson, R. S., Anderson, S. P., & Tucker, G. E. (2013). Rock damage and regolith transport by frost: An example of climate modulation of the geomorphology of the critical zone. *Earth Surface Processes and Landforms*, *38*, 299–316. https://doi.org/10.1002/esp.3330

Anderson, R. S., Rajaram, H., & Anderson, S. P. (2019). Climate driven coevolution of weathering profiles and hillslope topography generates dramatic differences in critical zone architecture. *Hydrological Processes*, *33*, 4–19. https://doi.org/10.1002/hyp.13307

Andrews, D. M., Lin, H., Zhu, Q., Jin, L. X., & Brantley, S. L. (2011). Hot spots and hot moments of dissolved organic carbon export and soil organic carbon storage in the Shale Hills Catchment. *Vadose Zone Journal*, *10*(3), 943–954. https://doi.org/10.2136/vzj2010.0149

Befus, K. M., Sheehan, A. F., Leopold, M., Anderson, S. P., & Anderson, R. S. (2011). Seismic constraints on critical zone architecture, Boulder Creek Watershed, Front Range, Colorado. *Vadose Zone Journal*, *10*, 915–927. https://doi.org/10.2136/vzj2010.0108

Brantley, S. L., Goldhaber, M. B., & Ragnarsdottir, K. V. (2007). Crossing disciplines and scales to understand the Critical Zone. *Elements*, *3*, 307–314. https://doi.org/10.2113/gselements.3.5.307

Brantley, S. L., Holleran, M. E., Jin, L. X., & Bazilevskaya, E. (2013). Probing deep weathering in the Shale Hills Critical Zone Observatory, Pennsylvania (USA): The hypothesis of nested chemical reaction fronts in the subsurface. *Earth Surface Processes and Landforms*, *38*, 1280–1298. https://doi.org/10.1002/esp.3415

Brantley, S. L., & Lebedeva, M. I. (2020). Relating land surface, water table, and weathering fronts with a conceptual valve model for headwater catchments. *Hydrological Processes*, *35*, e14010. https://doi.org/10.1002/hyp.14010

Brantley, S. L., Lebedeva, M. I., Balashov, V. N., Singha, K., Sullivan, P. L., & Stinchcomb, G. (2017). Toward a conceptual model relating chemical reaction fronts to water flow paths in hills. *Geomorphology*, *277*, 100–117. https://doi.org/10.1016/j.geomorph.2016.09.027

Brantley, S. L., & White, A. F. (2009). Approaches to modeling weathered regolith. In E. H. Oelkers, & J. Schott (Eds.), *Thermodynamics and kinetics of water–rock interaction*. *Reviews in Mineralogy and Geochemistry* (pp. 435–484). Mineralogical Society of America. https://doi.org/10.1515/9781501508462-012

Brantley, S. L., White, T., West, N., Williams, J. Z., Forsythe, B., Shapich, D., et al. (2018). Susquehanna Shale hills critical zone observatory: Shale Hills in the context of Shaver's Creek watershed. *Vadose Zone Journal*, *17*, 1–19. https://doi.org/10.2136/vzj2018.04.0092

Clark, G. M., & Ciolkosz, E. J. (1988). Periglacial geomorphology of the Appalachian highlands and interior highlands south of the glacial border–A review. *Geomorphology*, *1*, 191–220. https://doi.org/10.1016/0169-555x(88)90014-1

Dumbser, M., & Käser, M. (2006). An arbitrary high order discontinuous galerkin method for elastic waves on unstructured meshes II: The three-dimensional isotropic case. *Geophysical Journal International*, *167*(1), 319–336. https://doi.org/10.1111/j.1365-246X.2006.03120.x

Dunne, T. (1990). Hydrology, mechanics, and geomorphic implications of erosion by subsurface flow. In C. G. Higgins, & D. R. Coates (Eds.), *Groundwater Geomorphology: The Role of Subsurface Water in Earth-Surface Processes and Landforms* (Vol. 252, pp. 1–28). Geological Society of America, Special Paper. https://doi.org/10.1130/spe252-p1

Eppes, M.-C., & Keanini, R. (2017). Mechanical weathering and rock erosion by climate- dependent subcritical cracking. *Reviews of Geophysics*, *55*, 470–508. https://doi.org/10.1002/2017rg000557

Fichtner, A., Kennett, B. L. N., Igel, H., & Bunge, H.-P. (2009). Full seismic waveform tomography for upper-mantle structure in the Australasian region using adjoint methods. *Geophysical Journal International*, *179*(3), 1703–1725. https://doi.org/10.1111/j.1365-246X.2009.04368.x

Flinchum, B. A., Holbrook, W. S., Grana, D., Parsekian, A. D., Carr, B. J., Hayes, J. L., & Jiao, J. (2018). Estimating the water holding capacity of the critical zone using near-surface geophysics. *Hydrological Processes*, *32*(22), 3308–3326. https://doi.org/10.1002/hyp.13260

Fu, L., & Hanafy, S. M. (2017). *Ray-Tracing Traveltime Tomography Versus Wave-Equation Traveltime Inversion For Near-Surface Seismic Land Data. Interpretation 5: SO11–SO19* (Vol. 5, pp. SO11–SO19). https://doi.org/10.1190/INT-2016-0210.1

Ganor, J., Reznik, I. J., & Rosenberg, Y. O. (2009). Organics in water–rock interactions. *Reviews in Mineralogy and Geochemistry*, *70*, 259–369. https://doi.org/10.2138/rmg.2009.70.7

Graham, R. C., Rossi, A. M., & Hubbert, R. (2010). Rock to regolith conversion: Producing hospitable substrates for terrestrial ecosystems. *Geological Society of America Today*, *20*(2), 4–9. https://doi.org/10.1130/gsat57a.1

Gu, X., Mavko, G., Ma, L., Oakley, D., Accardo, N., Carr, B. J., et al. (2020). Seismic refraction tracks porosity generation and possible CO_2 production at depth under a headwater catchment. *Proceedings of the National Academy of Sciences of the United States of America*, *117*(32), 18991–18997. https://doi.org/10.1073/pnas.2003451117

Gu, X., Rempe, D. M., Dietrich, W. E., West, A. J., Lin, T.-C., Jin, L., & Brantley, S. L. (2020). Chemical reactions, porosity, and microfracturing in shale during weathering: The effect of erosion rate. *Geochimica et Cosmochimica Acta*, *269*, 63–100. https://doi.org/10.1016/j.gca.2019.09.044

Harman, C. J., & Cosans, C. L. (2019). A low-dimensional model of bedrock weathering and lateral flow coevolution in hillslopes: 2. Controls on weathering and permeability profiles, drainage hydraulics, and solute export pathways. *Hydrological Processes*, *33*, 1168–1190. https://doi.org/10.1002/hyp.13385

Holbrook, W. S., Riebe, C. S., Elwaseif, M., Hayes, J. L., Reeder, K., Harry, D. L., et al. (2014). Geophysical constraints on deep weathering and water storage potential in the Southern Sierra Critical Zone Observatory. *Earth Surface Processes and Landforms*, *39*(3), 366–380. https://doi.org/10.1002/esp.3502

Iverson, R. M., & Reid, M. E. (1992). Gravity-driven groundwater flow and slope failure potential, 1. Elastic effective-stress model. *Water Resources Research*, *28*(3), 925–938. https://doi.org/10.1029/91wr02694

Jin, L., Andrews, D. M., Holmes, G. H., Lin, H., & Brantley, S. L. (2011). Opening the "black box": Water chemistry reveals hydrological controls on weathering in the Susquehanna Shale Hills Critical Zone Observatory. *Vadose Zone Journal*, *10*, 928–942. https://doi.org/10.2136/vzj2010.0133

Jin, L., & Brantley, S. L. (2011). Soil chemistry and shale weathering on a hillslope influenced by convergent hydrologic flow regime at the Susquehanna/Shale Hills Critical Zone Observatory. *Applied Geochemistry*, *26*(Supplement), S51–S56. https://doi.org/10.1016/j.apgeochem.2011.03.027

Jin, L., Ravella, R., Ketchum, B., Bieman, P. R., Heaney, P., White, T., & Brantley, S. L. (2010). Mineral weathering and elemental transport during hillslope evolution at the Susquehanna/Shale Hills Critical Zone Observatory. *Geochimica et Cosmochimica Acta*, *74*, 3669–3691. https://doi.org/10.1016/j.gca.2010.03.036

Käser, M., & Dumbser, M. (2006). An arbitrary high order discontinuous Galerkin method for elastic waves on unstructured meshes I: The two-dimensional isotropic case with external source terms. *Geophysical Journal International*, *166*(2), 855–877. https://doi.org/10.1111/j.1365-246X.2006.03051.x

Keifer, I., Dueker, K., & Chen, P. (2019). Ambient Rayleigh wave field imaging of the critical zone in a weathered granite terrane. *Earth and Planetary Science Letters*, *510*, 198–208. https://doi.org/10.1016/j.epsl.2019.01.015

Lebedeva, M. I., & Brantley, S. L. (2013). Exploring geochemical controls on weathering and erosion of convex hillslopes: Beyond the empirical regolith production function. *Earth Surface Processes and Landforms*, *38*, 1793–1807. https://doi.org/10.1002/esp.3424

Lebedeva, M. I., & Brantley, S. L. (2020). Relating the depth of the water table to depth of weathering. *Earth Surface Processes and Landforms*, *45*, 2167–2178. https://doi.org/10.1002/esp.4873

Lee, E. J., Chen, P., Jordan, T. H., Maechling, P. B., Denolle, M. A., & Beroza, G. C. (2014). Full-3-D tomography for crustal structure in southern California based on the scattering-integral and the adjoint-wavefield methods. *Journal of Geophysical Research: Solid Earth*, *119*(8), 6421–6451. https://doi.org/10.1002/2014jb011346

Lin, H., Kogelmann, W., Walker, C., & Bruns, M. A. (2006). Soil moisture patterns in a forested catchment: A hydropedological perspective. *Geoderma*, *131*, 345–368. https://doi.org/10.1016/j.geoderma.2005.03.013

Liu, H., & Lin, H. (2015). Frequency and control of subsurface preferential flow: From pedon to catchment scales. *Soil Science Society of America Journal*, *79*(2), 362–377. https://doi.org/10.2136/sssaj2014.08.0330

Luo, Y., & Schuster, G. T. (1991). Wave-equation traveltime inversion. *Geophysics*, *56*, 645–653. https://doi.org/10.1190/1.1443081

Ma, L., Chabaux, F., West, N., Kirby, E., Jin, L., & Brantley, S. (2013). Regolith production and transport in the Susquehanna Shale Hills Critical Zone Observatory, Part 1: Insights from U-series isotopes. *Journal of Geophysical Research: Earth Surface*, *118*, 722–740. https://doi.org/10.1002/jgrf.20037

Ma, L., Oakley, D., Nyblade, A., Moon, S., Accardo, N., Wang, W., et al. (2021). Seismic imaging of a shale landscape under compression shows limited influence of topography-induced fracturing. *Geophysical Research Letters*, *48*, e2021GL093372. https://doi.org/10.1029/2021GL093372

Moon, S., Perron, J. T., Martel, S. J., Goodfellow, B. W., Mas Ivars, D., Hall, A., et al. (2020). Present-day stress field influences bedrock fracture openness deep into the subsurface. *Geophysical Research Letters*, *47*(23), e2020GL090581. https://doi.org/10.1029/2020gl090581

Nur, A., & Simmons, G. (1969). The effect of saturation on velocity in low porosity rocks. *Earth and Planetary Science Letters*, *7*, 183–193. https://doi.org/10.1016/0012-821X(69)90035-1

Parsekian, A. D., Singha, K., Minsley, B. J., Holbrook, W. S., & Slater, L. (2015). Multiscale geophysical imaging of the critical zone. *Reviews of Geophysics*, *53*, 1–26. https://doi.org/10.1002/2014rg000465

Perron, J. T., Richardson, P. W., Ferrier, K. L., & Lapôtre, M. (2012). The root of branching river networks. *Nature*, *492*(7427), 100–103. https://doi.org/10.1038/nature11672

Rempe, D. M., & Dietrich, W. E. (2014). A bottom-up control on fresh-bedrock topography under landscapes. *Proceedings of the National Academy of Sciences of the United States of America*, *111*, 6576–6581. https://doi.org/10.1073/pnas.1404763111

Riebe, C. S., Hahm, W. J., & Brantley, S. L. (2017). Controls on deep critical zone architecture: A historical review and four testable hypotheses. *Earth Surface Processes and Landforms*, *42*, 128–156. https://doi.org/10.1002/esp.4052

Roering, J. J., Kirchner, J. W., & Dietrich, W. E. (1999). Evidence for nonlinear, diffusive sediment transport on hillslopes and implications for landscape morphology. *Water Resources Research*, *35*, 853–870. https://doi.org/10.1029/1998wr900090

St. Clair, J., Moon, S., Holbrook, W. S., Perron, J. T., Riebe, C. S., Martel, S. J., et al. (2015). Geophysical imaging reveals topographic stress control of bedrock weathering. *Science*, *350*, 534–538. https://doi.org/10.1126/science.aab2210

Sullivan, P. L., Goddéris, Y., Shi, Y., Gu, X., Schott, J., Hasenmueller, E. A., et al. (2019). Exploring the effect of aspect to inform future earthcasts of climate-driven changes in weathering of shale. *Journal of Geophysical Research: Earth Surface*, *124*, 974–993. https://doi.org/10.1029/2017JF004556

Sullivan, P. L., Hynek, S., Gu, X., Singha, K., White, T. S., West, N., et al. (2016). *Oxidative dissolution under the channel leads geomorphological evolution at the Shale hills catchment*. American Journal of Science December. (pp. 981–1026). https://doi.org/10.2475/10.2016.02

Tape, C., Liu, Q., Maggi, A., & Tromp, J. (2009). Adjoint Tomography of the Southern California Crust. *Science*, *325*(5943), 988–992. https://doi.org/10.1126/science.1175298

Tarantola, A. (1988). Theoretical background for the inversion of seismic waveforms including elasticity and attenuation. *Pure and Applied Geophysics*, *128*(1–2), 365–399. https://doi.org/10.1007/BF01772605

Tromp, J., Tape, C., & Liu, Q. (2005). Seismic tomography, adjoint methods, time reversal and banana-doughnut kernels. *Geophysical Journal International*, *160*(1), 195–216. https://doi.org/10.1111/j.1365-246X.2004.02453.x

Wang, W., Chen, P., Dueker, K., Lee, E., Mu, D., & Keifer, I. (2020). Seismic evidence of glacial deposits inhibiting weathering of local bedrock at a snow-dominated subalpine watershed. *Earth and Planetary Science Letters*, *549*, 116517. https://doi.org/10.1016/j.epsl.2020.116517

Wang, W., Chen, P., Keifer, I., Dueker, K., Lee, E., Mu, D., et al. (2019). Weathering front under a granite ridge revealed through full-3D seismic ambient-noise tomography. *Earth and Planetary Science Letters*, *509*, 66–77. https://doi.org/10.1016/j.epsl.2018.12.038

West, A. J. (2012). Thickness of the chemical weathering zone and implications for erosional and climatic drivers of weathering and for carbon-cycle feedbacks. *Geology*, *40*, 811–814. https://doi.org/10.1130/g33041.1

West, N., Kirby, E., Bierman, P., & Clarke, B. A. (2014). Aspect-dependent variations in regolith creep revealed by meteoric ^{10}Be. *Geology*, *42*(6), 507–510. https://doi.org/10.1130/g35357.1

West, N., Kirby, E., Bierman, P., Slingerland, R., Ma, L., Rood, D., & Brantley, S. (2013). Regolith production and transport at the Susquehanna Shale Hills Critical Zone Observatory, Part 2: Insights from meteoric 10Be. *Journal of Geophysi- cal Research*, *118*, 1877–1896. https://doi.org/10.1002/jgrf.20121

West, N., Kirby, E., Nyblade, A., & Brantley, S. L. (2019). Climate preconditions the Critical Zone: Elucidating the role of subsurface fractures in the evolution of asymmetric topography. *Earth and Planetary Science Letters*, *513*, 197–205. https://doi.org/10.1016/j.epsl.2019.01.039., v.

Williamson, P. (1991). A guide to the limits of resolution imposed by scattering in ray tomography. *Geophysics*, *56*, 202–207. https://doi.org/10.1190/1.1443032

Yesavage, T. A., Fantle, M. S., Vervoort, J., Mathur, R., Jin, L., Liermann, L. J., & Brantley, S. L. (2012). Fe cycling in the Shale Hills Critical Zone Observatory, Pennsylvania: An analysis of biogeochemical weathering and Fe isotope fractionation. *Geochimica et Cosmochimica Acta*, *99*, 18–38. https://doi.org/10.1016/j.gca.2012.09.029